The Journal of Chemical Physics

RESEARCH ARTICLE | MAY 15 2023

Depletion-driven antiferromagnetic, paramagnetic, and ferromagnetic behavior in quasi-two-dimensional buckled colloidal solids

Analisa Hill ✉; Michio Tanaka; Kevin B. Aptowicz; ... et. al

Check for updates

J. Chem. Phys. 158, 194903 (2023)
https://doi.org/10.1063/5.0146155

View Online
Export Citation
CrossMark

Articles You May Be Interested In

Buckling resistant graphene nanocomposites

Appl. Phys. Lett. (December 2009)

Buckling of a columnar vortex

Physics of Fluids A: Fluid Dynamics (December 1992)

Buckling of defective carbon nanotubes

Journal of Applied Physics (December 2009)

AIP Publishing

The Journal of Chemical Physics
ARTICLE
scitation.org/journal/jcp

Depletion-driven antiferromagnetic, paramagnetic, and ferromagnetic behavior in quasi-two-dimensional buckled colloidal solids

Cite as: J. Chem. Phys. 158, 194903 (2023); doi: 10.1063/5.0146155
Submitted: 10 February 2023 • Accepted: 10 April 2023 •
Published Online: 15 May 2023

Analisa Hill,[1,a)] Michio Tanaka,[1] Kevin B. Aptowicz,[2] Chandan K. Mishra,[3] A. G. Yodh,[1] and Xiaoguang Ma[4,5,a)]

AFFILIATIONS

[1] Department of Physics and Astronomy, University of Pennsylvania, Philadelphia, Pennsylvania 19104, USA
[2] Department of Physics and Engineering, West Chester University, West Chester, Pennsylvania 19383, USA
[3] Discipline of Physics, Indian Institute of Technology (IIT) Gandhinagar, Palaj, Gujarat 382055, India
[4] Center for Complex Flows and Soft Matter Research, Southern University of Science and Technology, Shenzhen, Guangdong 518055, China
[5] Department of Physics, Southern University of Science and Technology, Shenzhen, Guangdong 518055, China

[a)] **Authors to whom correspondence should be addressed:** anahill@sas.upenn.edu and maxg@sustech.edu.cn

ABSTRACT

We investigate quasi-two-dimensional buckled colloidal monolayers on a triangular lattice with tunable depletion interactions. Without depletion attraction, the experimental system provides a colloidal analog of the well-known geometrically frustrated Ising antiferromagnet [Y. Han *et al.*, Nature **456**, 898–903 (2008)]. In this contribution, we show that the added depletion attraction can influence both the magnitude and sign of an Ising spin coupling constant. As a result, the nearest-neighbor Ising "spin" interactions can be made to vary from antiferromagnetic to para- and ferromagnetic. Using a simple theory, we compute an effective Ising nearest-neighbor coupling constant, and we show how competition between entropic effects permits for the modification of the coupling constant. We then experimentally demonstrate depletion-induced modification of the coupling constant, including its sign, and other behaviors. Depletion interactions are induced by rod-like surfactant micelles that change length with temperature and thus offer means for tuning the depletion attraction *in situ*. Buckled colloidal suspensions exhibit a crossover from an Ising antiferromagnetic to paramagnetic phase as a function of increasing depletion attraction. Additional dynamical experiments reveal structural arrest in various regimes of the coupling-constant, driven by different mechanisms. In total, this work introduces novel colloidal matter with "magnetic" features and complex dynamics rarely observed in traditional spin systems.

I. INTRODUCTION

Over the years, experiments with model colloidal suspensions have generated fundamental insights about melting in two- and three-dimensions (2D and 3D),[2–7] crystal physics,[8–10] nucleation kinetics,[11–16] and the nature and mechanics of disordered solids (glasses).[17–28] These investigations with colloids are complementary to studies of atomic systems because the length- and time-scales in suspension permit direct visualization and tracking of constituents with single-particle resolution.[29] Such studies often unify the soft- and hard-matter phenomenology and explore ideas from statistical mechanics.

One fascinating model system along these lines is the buckled colloidal monolayer,[30–37] which consists of a packing of colloidal particles confined by two walls whose separation is ∼1.5 particle diameters. This quasi-2D buckled monolayer of particles on a triangular lattice provides a colloidal analog of the classic frustrated antiferromagnetic Ising model, which was first studied by Wannier[38] and has been realized in a variety of experiments and simulations.[39–66] In this system, up and down out-of-plane particle displacements are analogous to Ising spins that point, respectively, up and down; the free volume (entropy) of each particle depends on the out-of-plane position of its nearest neighbors and is maximum when neighboring particles buckle in opposite directions. Moreover, by varying the colloid sphere diameter while holding wall separation constant, it is possible to tune nearest-neighbor free-volume differences and thereby vary the effective antiferromagnetic coupling constant. Experiments and theory based on this colloidal system have probed "spin" configurations, "spin" dynamics, and lattice distortions as a function of interaction strength and frustration.[1,55,67–72]

In this contribution, we introduce a quasi-2D buckled monolayer system that enables tuning of the sign and magnitude of the Ising spin coupling constant *in situ*. As a result, the nearest-neighbor "spin" interactions can vary from antiferromagnetic to para- and ferromagnetic. We demonstrate this basic phenomenon in experiments that employ suspensions of nearly hard-sphere particles of fixed diameter and rod-like micelles whose length can be tuned by varying temperature.[73–76] The rod-like micelles induce a short-range depletion attraction between nearest-neighbor particle pairs with attraction strength that varies with micelle length; this depletion force is nearly zero at low temperature, large at high temperature, and monotonic in-between. The effective Ising coupling constant is set by a combination of the original antiferromagnetic free volume effect (without depletion), which prefers oppositely buckled neighbors, and the depletion attraction, which prefers neighbors with the same buckling. By using temperature to tune depletion attraction strength, we demonstrate modulation of the effective Ising coupling constant, even changing its sign, and we generate experimental state diagrams for the system. We also measure particle dynamics, i.e., spin-flip autocorrelation functions as a function of depletion attraction strength.

In parallel, we develop theoretical models to elucidate these effects. A comparison of the experiment and the simplest theory not only corroborates major concepts but also reveals complexities of the colloid system beyond what can be described by the simplest models. Depletion-driven wall interactions, for example, affect energetics and kinetics and introduce new physics. Therefore, for comparison with the experiment, we incorporate some of these features into a more sophisticated and realistic theoretical model, which we use to calculate phase diagrams as a function of temperature, packing, and the ratio of cell-thickness to particle-diameter. In total, this work takes first steps toward the creation of colloidal matter with "magnetic" features rarely observed in traditional atomic systems. In addition to equilibrium behavior, the experiments initiate the investigation of the microscopic kinetics and non-equilibrium dynamics of the "magnetic" colloidal matter.

The remainder of this paper is organized as follows. Section II A introduces the central concept with a very simple hard-sphere model in quasi-1D; this model shows how the Ising coupling constant can be tuned from antiferromagnetic to the para- and ferromagnetic regimes via the modification of geometrical parameters and short-range depletion attraction. Then, we introduce and discuss more comprehensive quasi-2D models with and without wall attraction; these models provide context for an experimental comparison. Section III details the experimental methods. Section IV presents the primary experimental phase-diagram and quantitative results and briefly discusses dynamical observations. Section V summarizes the findings and suggests directions for future work.

II. THEORY

A. Quasi 1D: Introduction to basic effect

Here, we introduce a simple model first developed for hard-spheres that we generalize to include arbitrary interparticle potentials. The simple model serves to clarify the physical concepts, especially how the Ising coupling constant varies with depletion attraction strength. In Sec. II B, we develop a realistic model that captures more features of our experimental system, including its many-body free energy; using the realistic model, we work out phase diagrams with and without wall interactions. For the reader who is not interested in detailed modeling, we recommend perusing the phase diagrams in Sec. II B and then skipping to Secs. III and IV.

The experiments employ hard-sphere colloidal particles arranged on a triangular lattice in the xy-plane (the transverse plane) with in-plane nearest-neighbor spacing, L; the particles have diameter D (see Fig. 1). The particles are confined vertically by two walls, i.e., confined in the out-of-plane z-direction. The wall separation (sample thickness) is H. Typically, the thickness-to-diameter ratio, H/D, is ∼ 1.5 or smaller, and the system volume fraction is nearly closed-packed. We first analyze the colloidal system without depletion interactions (closely following prior work[1,68]); then, we add small micellar depletants into the system and elucidate new features.

With only hard-core repulsive interactions between spheres (and between spheres and walls), the particles seek to maximize their free volume or translational entropy. Thus, neighboring particles tend to move out-of-plane (buckle) in opposite directions. We coarse grain single-particle microstates with the particle center above and below the lattice plane, respectively, into the "up" and "down" macrostates. We assign to each particle a spin value of +1 if the z-component of the particle's position is above the mid-plane of the sample cell ($z = H/2$) and a spin value of −1 otherwise. Qualitatively, nearest neighbors behave like Ising spins that interact antiferromagnetically with a coupling constant, J. Specifically, the interaction energy between neighboring particles is $-Js_is_j$, where s_i and s_j denote the spins assigned to particles i and j and $J < 0$. Generally, we will employ this theoretical model (or more complex versions of the model) to find a spin coupling constant J such that the free energy of the particle lattice best resembles the energy of an Ising lattice with an equivalent spin configuration $\{s_i\}$. Previous work, which reduced the many-body partition function to a single-particle one, has shown for hard-spheres that J quantitatively depends on H/D and L/D.[1,67,68]

We next generalize this theoretical approach[67,68] to include interparticle interactions beyond that of hard spheres. Specifically, we will show how short-range attractive interactions between spheres due to added depletants can cause the sign and magnitude of J to change.

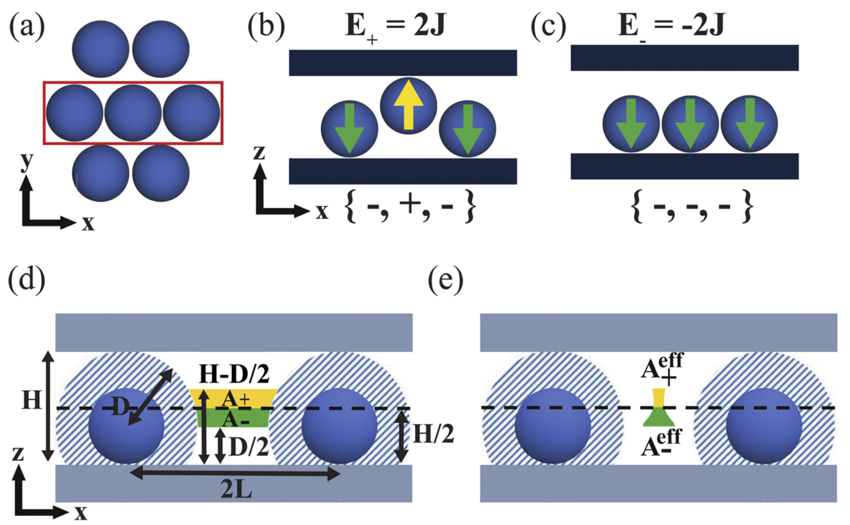

FIG. 1. Quasi-1D model. (a) (Top-down view) A particle and its nearest neighbors in quasi-2D. The red rectangle outlines the central particle and two equally spaced neighbors in quasi-1D. (b) and (c) (Side view) Correspondence between Ising spins and the particle z-position. In (b), the central particle is buckled out-of-plane in the vertical direction; $\{- + -\}$ describes the configuration with the "up" central particle spin state. In (c), $\{- - -\}$ describes the configuration with the "down" central particle spin state. (d) and (e) (Side views) Free areas associated with "up" and "down" states of the central particle. The central particle's free area, A_+ (A_-), is shown in yellow (green), when buckled up (down). The edge of the lower (upper) wall is at $z = 0$ ($z = H$). The black dashed line at $z = H/2$ separates up/down free areas. Dark blue circles represent the cores of the central particle's nearest neighbors (with center-to-center separation, $2L$). Light blue circles represent areas inaccessible to the geometric center of the *central* particle. $x = 0$ is located midway between the outer particles.

The analysis builds on the quasi-1D model of Shokef and coworkers for confined and frustrated colloidal Ising antiferromagnets on a triangular lattice.[67,68] This quasi-1D model focuses on three particles in the hexagonal cell [collinear particles enclosed by a red rectangle in Fig. 1(a)] and computes the relative free area (or free volume) of the *central* particle in its up vs down state. The microstate of the ith particle is specified by its position in the xz-plane, (x_i, z_i); the system microstate involves all particles $(1 \le i \le N)$ on the lattice.

The colloid problem is next transformed to a corresponding problem with Ising-like spin configurations. Each particle i is specified by the z-component of its "spin" s_i, where $s_i = \pm 1$. Here, x describes the in-plane position of the central particle ($x = 0$ corresponds to the horizontal position of the center of the central particle located midway between the outer particles); z is the out-of-plane position of the central particle constrained by walls at $z = 0$ and $z = H$. When a particle is above (below) the vertical center of the cell $(z = H/2)$, it is in the spin-up (spin-down) state, $s_i = +1$ ($s_i = -1$). Note that if the central particle's two outer neighbors are in opposite spin states, e.g., $\{- - +\}$ or $\{- + +\}$, then the accessible areas associated with the central particle being up vs down are equal. However, when two neighbors are in the same spin state, e.g., both spin-down, then the buckled-up central particle, $\{- + -\}$, has more free area [shaded yellow, Fig. 1(b)] than a buckled-down central particle $\{- - -\}$ [shaded green, Fig. 1(c)].

Shokef and Lubensky[67] showed that this hard-sphere system has an effective antiferromagnetic interaction $(J < 0)$ with

$$\beta J = -\frac{1}{4}\ln\left(\frac{A_+}{A_-}\right) < 0. \tag{1}$$

Here, $\beta \equiv 1/k_B T$, k_B is the Boltzmann constant, T is the temperature, and A_+ (A_-) is the free area available to the central particle when it resides in a vertical plane opposite from (the same as) its two neighbors; see Fig. 1(d). The coupling constant, J, can be changed in magnitude by modifying system geometry, i.e., H, D, and L. Although approximate, this model largely accounts for observed phenomena.[1] If we permit lattice distortion, the model also elucidates stripe and zigzag spin configurations observed experimentally.[1,55]

We next extend the quasi-1D model to the more general situation wherein interparticle interactions are different from hard-spheres. For clarity, the analysis will focus on the case where both outer neighbors are in spin-down states [Fig. 1(d)].

Consider the probability for the central particle to be either spin-up or spin-down. Then, the probability of the central particle i being in a particular "spin" configuration is

$$p(s_i; H, D, L) = \mathscr{Z}(s_i; H, D, L)/\mathscr{Z}. \tag{2}$$

$\mathscr{Z}(\pm 1; H, D, L)$ is the integral of the Boltzmann weight over the accessible area, $A_\pm$, of the central particle in the up/down spin state. The "total" partition function is

$$\mathscr{Z} \equiv \mathscr{Z}(+1; H, D, L) + \mathscr{Z}(-1; H, D, L). \tag{3}$$

It is needed for normalization.

More explicitly, the numerators in Eq. (2) are

$$\mathscr{Z}(+1;\, H, D, L) = \mathscr{C}\int_{H/2}^{H-D/2} 2\int_{0}^{x_{max}(z)} e^{-\beta U(x,z)}\, dx\, dz, \tag{4}$$

$$\mathscr{Z}(-1;\, H,D,L) = \mathscr{C}\int_{D}^{H/2} 2\int_{0}^{x_{max}(z)} e^{-\beta U(x,z)}\, dx\, dz. \tag{5}$$

The constant $\mathscr{C}$ accounts for the contribution of the integration over momentum and other constants. The integrand in Eqs. (4) and (5) contains a Boltzmann factor involving the potential energy, $U(x,z)$, felt by the central particle due to its two neighbors. In contrast to the hard-sphere case, these potentials can be non-zero even when the central particle does not overlap physically with neighboring particles (or walls). The upper limit, $x_{\max}(z)$, represents the maximum in-plane displacement the particles can have such that they do not overlap physically with their neighbors; $x_{max}(z)$ is a function of the out-of-plane (vertical) position, z. (Note that we integrate over positive x and account for the bilateral symmetry with a factor of 2.)

In the hard-sphere case (without depletants), $U(x,z) = 0$ within the accessible area of the central particle. Therefore, the value of the Boltzmann weight becomes unity and Eqs. (4) and (5) become the total accessible area to the central particle in the up and down spin state, respectively. Accordingly, the probability that the central particle resides in an up spin state is

$$\mathscr{Z}(+1; H,D,L)/\mathscr{Z} = A_+/A_{tot}, \tag{6}$$

and the probability that the central particle resides in a down-spin state is

$$\mathscr{Z}(-1; H,D,L)/\mathscr{Z} = A_-/A_{tot}. \tag{7}$$

$A_{tot} \equiv A_+ + A_-$ is the total free area available to the central particle. The Ising coupling constant, J, is determined from the ratio of accessible free areas,

$$\frac{p(+1)}{p(-1)} = \frac{e^{-2\beta J}}{e^{2\beta J}} = \frac{A_+}{A_-}. \tag{8}$$

Rearrangement of this equation gives Eq. (1).

We next include depletion interactions in Eqs. (4) and (5). In the experiments, rod-like surfactant micelles are employed as depletants, and we control the strength and range of the depletion interaction by tuning the rod length (see Fig. 2 and Sec. III for details). Importantly, the numerical values of the Boltzmann weights will no longer be either zero or unity. The depth of the depletion attraction potential is an increasing function of the depletant volume-fraction ϕ_d, which (in practice) can be made roughly constant; the depth is also an increasing function of cylinder major axis length, ℓ, which can be controlled by temperature.

An analytical expression for this depletion potential has been worked out[77] and can be written in the following form:

$$\beta U^{attr}(r; \ell, d, R, \phi_d) = \phi_d \frac{R\ell}{d^2} Q(r; \ell, d). \tag{9}$$

The function $Q(r;\ \ell, d)$ is given in the supplementary material, Sec. S1. The colloidal particle radius is $R = D/2$. $U^{attr}(r;\ \ell, d, R, \phi_d)$ is infinite when particles touch, zero at long range, and *negative* when particle surfaces are separated by a distance less than $\sim\ell$. Thus, $U(x,z)$ need not be zero, and the Boltzmann weight need not be unity when the particles do not physically overlap. In this case, Boltzmann integrals will no longer give true physical areas.

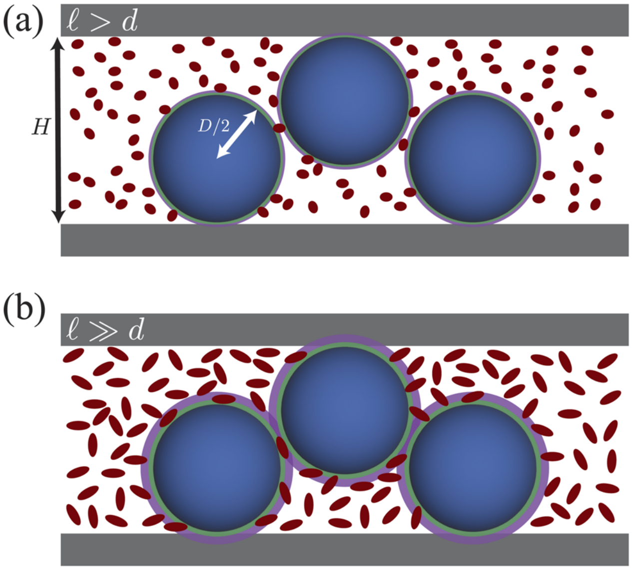

FIG. 2. Schematic illustrating the depletion interaction between colloidal particles of radius $R = D/2$ in a suspension of rod-like micelles with major axis length ℓ, minor axis length d, and fixed micelle volume fraction ϕ_d. The depletion attraction effect arises because the micelles cannot reside in regions of excluded volume (light purple regions surrounding the colloidal particles). Unlike spherical depletants, rods can be excluded from the shaded regions due to their center-of-mass position and/or due to the orientation of their major axis. These effects are approximately captured in the schematic. The purple shaded region extends radially by half the rod major-axis length from the large sphere surface. Rods with center-of-mass located at the edge of this region can lie along any angular orientation; rods with center-of-mass located inside the edge can only orient along a subset of angles. Note, further, that the rod center-of-mass can never reside at a location less than the half rod minor-axis length from the large sphere surface, which is represented by the green shaded region that extends radially from the large sphere surface. Thus, rods can exist in the overlapping excluded volumes of this image but only for a finite set of angular orientations. (a) At low temperature, ℓ and d are approximately equal, the micelles are nearly spherical, and the regions of excluded volume are very thin. (b) At higher temperatures, ℓ increases, but d does not change. The regions of excluded volume increase relative to (a); moreover, the pair-potential depth at contact also increases relative to (a).

As a result, we obtain a modified version of Eq. (1) that relates J to a ratio of *effective areas* defined by the integrals in Eqs. (4) and (5),

$$\beta J = -\frac{1}{4}\ln\left(\frac{A_+^{eff}}{A_-^{eff}}\right). \tag{10}$$

The ratio of *effective areas* is obtained by the evaluation of the integrals weighted by the depletion potential. In practice, at low temperature and relatively low volume-fraction [Fig. 2(a)], the rods are very short, and the interaction between the large particles (with diameter D) is hard-sphere-like. Then, $A_+^{eff}/A_-^{eff} \approx A_+/A_- > 1$ [Fig. 1(d)] and $J < 0$. The system is antiferromagnetic.

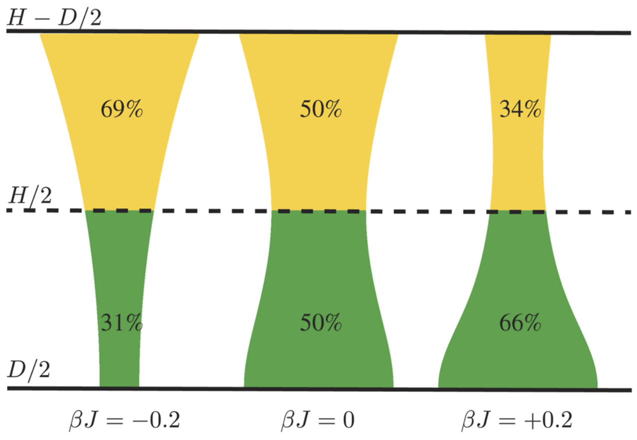

FIG. 3. Results of simple quasi-1D model calculations illustrate the temperature-dependent relationship between the Ising coupling constant and the ratio of effective areas. The yellow (green) region represents the effective area, from the Boltzmann-weighted integral, for a buckled-up (buckled-down) central particle. From left to right, ℓ is 4.3, 16.3, and 20 nm, respectively. For the calculations, we assumed a depletant volume fraction, ϕ = 0.0049; a depletant cylinder minor axis length, d = 4.3 nm; a colloidal particle diameter, D = 1.0 μm; and a ratio of lattice spacing to particle diameter, L/D = 1.01. The vertical axis corresponds to height (z) within the sample.

However, when the sample temperature increases [Fig. 2(b)], the rod length increases. When the rod length increases, the interparticle potential well-depth and the range of the potential increase. This effect causes the ratio of the effective areas to vary. At high temperature, the ratio $A_+^{eff}/A_-^{eff} < 1$ [Fig. 1(e)] and the Ising coupling constant $J > 0$. Thus, the sign of the effective Ising coupling constant can be changed from negative to positive by increasing the depletion interaction strength. This increasing nearest-neighbor particle interaction will thus transform the sample from antiferromagnetic to paramagnetic states (and to a ferromagnetic state when $\beta J \geq 0.275$; see Appendix C).

In Fig. 3, we display the results of numerical calculations based on this simple quasi-1D model with the depletion interaction due to cylindrical micelles at a fixed volume fraction. At low temperature, when the depletants are approximately small spheres, A_+^{eff}/A_-^{eff} gives a 69% (31%) probability of being buckled-up (buckled-down) and $\beta J < 0$. At slightly higher temperatures with the same volume fraction, the depletants become more rod-like, the effective areas become comparable, and $\beta J \approx 0$. Finally, when the micelles become long rods at high temperatures, the probability of the central particle buckling-up (buckling-down) is 34% (66%) and $\beta J > 0$. Thus, the simple model clearly suggests that depletion attraction facilitates variation of the Ising coupling constant from negative to positive values (passing through zero).

B. Realistic quasi-2D models, phase diagrams

1. Quasi-2D and bulk interactions

The quasi-1D model introduced in Sec. II A illustrates key concepts but has significant limitations. It ignored the many-body nature of the Hamiltonian of the particle system, and the model was quasi-1D. A more realistic calculation should extend this problem to three dimensions (3D) and should aim to recover system free energy contributions due to more degrees of freedom of the central particle neighbors (e.g., nearest and next-nearest neighbors). To this end, we extend the model to quasi-2D, we take into account the free energy of the central particle and its nearest neighbors, and we compute βJ from a statistical average over all the possible neighbor configurations, i.e., k possible configurations. To account for the free energy of the central particle and its nearest neighbors, we must include the state of all particles in the central particle's nearest and next-nearest neighbor rings; this gives 2^{18} possible values of k. For each k, an optimal J_k can be computed that is associated with the energy difference of the configuration k with the central particle buckled up vs down

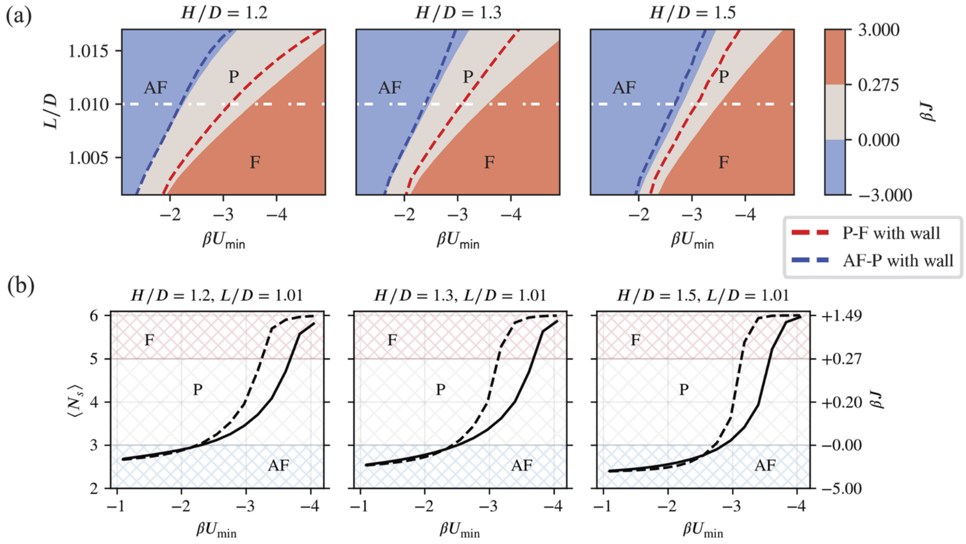

FIG. 4. (a) Quasi-2D phase diagrams for H/D = 1.2, 1.3, and 1.5, respectively. Blue color corresponds to the antiferromagnetic region (AF), beige corresponds to the paramagnetic region (P), and red corresponds to the ferromagnetic region (F). Red and blue dashed lines indicate the relatively small shift "where" transitions occur when depletion attractions to the wall are included. The blue (red) dashed line is the wall-induced shift for the AF–P (P–F) transition. The white dashed line indicates the constant L/D for which the curves in (b) are obtained. (b) Number of similar bonds $\langle N_s \rangle$ and βJ plotted as a function of depletion attraction strength $\beta U_{\min}$ at fixed L/D = 1.01. Black dashed (solid) lines indicate the behavior with (without) wall attractions.

(details in Appendix B). To compute the ensemble averaged J for the quasi-2D system, we average over all possible values of J_k,

$$J = \frac{\sum_k J_k w_k}{\sum_k w_k}, \qquad (11)$$

where w_k is the Boltzmann weight for observing the kth configuration. This approach incorporates the relative probability of observing each nearest-neighbor spin configuration.

We carried out these calculations computationally using the depletion potential for cylindrical micelles. Figure 4(a) shows predictions of this more realistic quasi-2D model as a function of depletion attraction strength (βU_{min}) and diameter-normalized lattice spacing (L/D) and cell thickness (H/D). βU_{min} increases from left-to-right in the plot; note that both the magnitude of the depletion attraction and the temperature increase moving left-to-right. The color scale in the phase diagrams corresponds to different regimes of the predicted Ising coupling constant. The blue region corresponds to the frustrated antiferromagnetic (AF) phase where $-3 < \beta J < 0$; beige corresponds to the paramagnetic phase (P) where $0 < \beta J < 0.275$, and red corresponds to the ferromagnetic phase (F) where $\beta J \geq 0.275$[78,79] (see also Appendix C). Generally, the system starts in the AF region at low temperature, where the depletion attraction is very small, and evolves from AF ($J < 0$) to P ($J > 0$) as the magnitude of the attractive depletion interaction increases. Note that, for fixed H/D, a larger depletion attraction is required to reach the (AF–P) crossover for increasing L/D. Note also that, for fixed L/D, a larger depletion attraction is required to reach the (AF–P) crossover for increasing H/D.

We quantitatively characterize "magnetic" order in the samples using the ensemble-averaged number of similar bonds, $\langle N_s \rangle$. Here, bonds refer to nearest-neighbor pairs involving particles i and j. A similar bond between two particles occurs when a particle and its neighbor are in the same Ising spin state ($s_i s_j = 1$); a dissimilar bond occurs when a particle and its neighbor are in opposite Ising spin states ($s_i s_j = -1$). Notably, $\langle N_s \rangle$ is a measurable and calculable parameter that helps identify the crossover from anti-to para-to ferromagnetic phases. $\langle N_s \rangle$ also helps distinguish strong vs weak coupling in samples with the same magnetic classification. In Fig. 5(a), all possible nearest-neighbor configurations for a central particle in the spin-up state are shown, and the number of similar bonds for the central particle is indicated. An equivalent set of configurations can be constructed for a central particle in the spin-down state. (As an aside, the term frustrated bond and the number of frustrated bonds, $\langle N_f \rangle$, are sometimes used in the literature; note that a similar bond is equivalent to a frustrated bond for spins in the *antiferromagnetic* phase.)

Figure 4(b) shows the relationship between $\langle N_s \rangle$, βJ, and βU_{min} for a fixed lattice spacing of $L/D = 1.01$ [indicated by the white dashed line in Fig. 4(a)]. To obtain these curves, theoretical parameters [$\beta U^{attr}(r;\ \phi_d, \ell, d)$, H/D, L/D] are input into our numerical model, and βJ is computed. This model prediction for the coupling constant, βJ, is then inserted into Wannier's analytic theory[38,80] to derive a value for $\langle N_s \rangle$. Theoretical curves, such as those in Fig. 4(b), will be used later [Fig. 5(b)] to characterize experimental data.

A few features from Fig. 5 are worth noting for future analysis. The realistic theory demonstrates that for smaller H/D, a smaller depletion attraction is needed to reach the AF–P crossover; it also explicitly reveals that the number of similar bonds increases rapidly in the paramagnetic regime. For larger H/D, a larger depletion attraction is required to reach the AF–P crossover; note also that, for larger H/D, a more gradual increase in $\langle N_s \rangle$ is found in the paramagnetic regime compared to smaller H/D. Qualitatively, these trends can be understood to be a consequence of the fractionally less close-particle-contact that arises as L/D and H/D increase; with a fractionally less close-particle-contact, the importance of the depletion attraction is reduced (since depletion occurs when particles are in close contact). Put another way, when particles have more room to move, then the influence of the short-range depletion attraction is reduced.

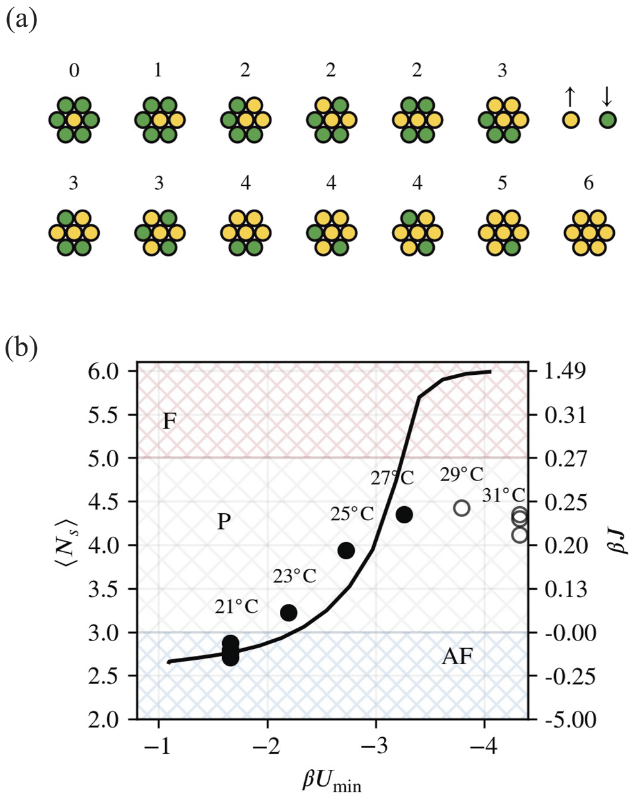

FIG. 5. (a) Configurations of a central particle and its nearest neighbors; the index indicates the number of similar bonds (neighbors with parallel spins). Due to the rotational and inversion symmetry, 13 distinct configurations arise. (b) Number of similar bonds $\langle N_s \rangle$ and βJ vs depletion attraction strength, $\beta U_{\min}$. The black line is theory from our quasi-2D model, including wall interactions; the theory specifies βJ vs $U_{\min}$ extracted from our quasi-2D model, including wall interactions, with parameters $H/D = 1.2$, $L/D = 1.01$, and $\phi_d = 0.0049$. Circles are the experimental data specified by the $\langle N_s \rangle$ vs $U_{\min}$ axes; black solid (open) circles indicate data from equilibrium (non-equilibrium) samples. Note that there is a 1:1 correspondence between the $\langle N_s \rangle$ and βJ vertical axes; they are vertically aligned so that the corresponding values of $\langle N_s \rangle$ and βJ arise in Wannier's theory under the same conditions.

2. Wall interactions

The presence of the wall introduces energetic changes, which can affect trends. In dilute systems, the particle–wall depletion attraction is approximately twice as strong as the depletion attraction between two particles in the bulk suspension; this effect has been measured and can be understood from purely geometric considerations.[73,81–84] This effect further modifies the ratio of effective free volumes (V_+^{eff}/V_-^{eff}) associated with buckling up vs down; for example, when all of the nearest neighbors are on the top wall, then the central particle will have access to a different patch of the physical area on the top wall compared to the bottom wall. This behavior tends to enhance the primary depletion effect discussed in Sec. II A (see the supplementary material, Fig. S4) and leads to a small shift in the crossover condition from one magnetic phase to another (see blue and red dashed lines in Fig. 4). Specifically, for the case where all of the central particle's nearest neighbors are up, the depletion effect is stronger for the particle on the top wall compared to the bottom wall. Therefore, the coupling constant βJ becomes more positive. As a result, the AF–P crossover region shifts to the left in the phase diagram (dashed lines in Fig. 4), indicating that the AF–P transition will occur at lower βU_{min} (lower temperature).

Since the phase diagram depends on the free energy difference, the basic features of the phase diagram are largely unchanged by the wall attraction. However, the energy barrier for a particle to escape from the wall, and thus flip from one wall to the other, is made much larger by the wall depletion attraction. As a result, the system dynamics will become slower with the increasing attraction strength. This phenomenon has important practical consequences for experiments, which we will discuss in Sec. IV.

III. EXPERIMENTAL METHODS

This section discusses the samples and experimental execution. In addition, we provide details about image analysis, image processing techniques, and measurements of interparticle potentials (depletion attraction strength).

A. Particles and particle preparation

The colloidal particles employed in the experiments were polystyrene microspheres (Thermo Fisher Scientific) with a manufacturer-measured diameter, $D = 1.0 \pm 0.01\ \mu$m. To prepare the sample, the microspheres were rinsed in ultrapure water $(18.2\ \text{M}\Omega)$, and aggregates were removed by repeated centrifugation. The cleaned particles were then resuspended in 55 mM aqueous solutions of the surfactant hexaethylene glycol monododecyl ether $(C_{12}E_6)$. $C_{12}E_6$ self-assembles into rod-like micelles with temperature-dependent length that permits for temperature-tuning of the depletion attraction between colloidal particles. NaCl was added to the solution at a concentration of 2 mM, which gives a Debye screening length of $\kappa^{-1} \approx 7$ nm.

B. Sample cell preparation and sample observation

Sample cells were constructed by sandwiching the suspension between two $20 \times 50\ \text{mm}^2$ glass coverslips (No. 1.5, 170 μm-thick, Electron Microscopy Sciences). The coverslips were cleaned to remove impurities from their surfaces by soaking each slip in base solution for >30 min. The base solution contained 5 g of sodium hydroxide (NaOH) in a solvent consisting of 20 ml of ultrapure water $(18.2\ \text{M}\Omega)$ and 30 ml of ethanol. After soaking, the coverslips were washed with ultrapure water and then with isopropyl alcohol, and finally, they were dried with compressed air.

The coverslips were separated/spaced via the application of two rows and three columns of UV glue drops (Norland adhesive 65) onto the bottom cover slip. After drying, the coverslips were aligned and sandwiched at a small angle; binding was achieved via capillary forces. Approximately 25 μl of the sample solution was pipetted into the sample cell, and then, the remaining peripheral openings were sealed. Finally, the resulting quasi-2D sample wedge-cell was mounted onto a glass slide for improved stability.

These sample cell units were imaged via transmission light microscopy on the stage of an inverted microscope (Leica DMIRB) and were viewed through a 100× oil-immersion objective. The sample temperature was controlled by a heater (peCon GmbH) on the objective, with 0.1 °C resolution. Colloidal particle positions and brightness (intensity) were collected by video microscopy using a CCD camera (UNIQ, UP-685-CL) with a resolution of 659× 494 pixels at a frame rate of 27.5 frames per second. Particle position and motions are analyzed with standard particle tracking methods and algorithms.[29]

C. Temperature-tunable depletion interparticle potentials and wall interactions

The depletion interaction potential between colloidal particles, $U(r)$, depends on the concentration and character of tiny suspended depletants. For the case of the $C_{12}E_6$ surfactant, the surfactant molecules self-assemble into micelles, and the geometric shape of these micelles affects both the strength and range of the depletion attraction.[73,76,81,84–86] Specifically, $C_{12}E_6$ assembles into nanometer-size micelles that evolve from sphere-like for $T < 20\ ^\circ$C to rod-like for $T > 20\ ^\circ$C.[76,87] The length of the micelle minor axis is $d = 4.3$ nm; it does not change with temperature. However, the micelle major axis length, ℓ, grows with the increasing temperature. This effect enables control of the attraction strength between colloidal particles *in situ*, which is critical for tuning the Ising coupling constant.

Experimentally, we derived the normalized depletion pair potential, $\beta U(r)$, from measurements of the radial distribution function, $g(r)$, in samples at low particle packing fraction $(\phi_p \sim 0.013)$. For analysis, we assumed $U(r) = -k_B T \ln g(r)$; use of dilute samples reduces the influence of many-body interactions and ameliorates the need to invert the data using integral equations. This procedure for extracting $\beta U(r)$ is outlined in detail for $C_{12}E_6$ by Gratale *et al.*[76] Figure S2 of the supplementary material displays the resulting data and shows that βU_{min}, the absolute value of the maximum attraction depth of $\beta U(r)$, becomes larger with the increasing temperature. Note that, even at our lowest temperature, the depletion attraction is non-zero; thus, the experimental conditions at low temperature differ somewhat from the expectations of our theoretical models.

Additionally, as described in Sec. II B 2, depletion interactions between walls and particles can become significant at high temperatures. The particle–wall attraction at contact is approximately twice that of between two particles in the bulk. This effect has a small influence on the equilibrium phase diagram. However, particles can also become kinetically arrested, i.e., because the energy barrier to escape from the wall is large. Our experiments revealed this kinetic arrest.

D. Average number of similar neighbor bonds ($\langle N_s \rangle$) and magnetic state

For system characterization and comparison of experiment to theory, we analyzed up/down spin data for the whole sample (see Appendix A). Specifically, from the images, we derived the average number of similar neighbor bonds, $\langle N_s \rangle$, and its variance. We found that $\langle N_s \rangle$-based metrics are robust to sample systematics compared to other possible variables. In the supplementary material, Sec. S2, we briefly describe some systematic effects that drove our decision to focus on $\langle N_s \rangle$.

E. Wall- and lattice-spacing measurements

The Ising coupling constant depends on the ratio of the wall- and lattice-spacing to the particle diameter (H/D and L/D). We discuss our procedures to measure H, D, L, H/D, and L/D in the supplementary material (Sec. S4). In practice, H/D for the different samples was 1.23 ± 0.08, 1.29 ± 0.08, and 1.55 ± 0.07. For L/D, the mean value averaged across samples was 1.01. The variation of H/D across the field-of-view is small (~5%); this leads to a relatively small variation of the coupling constant (±10%), which does not change any of our conclusions about systematic coupling constant variation and transitions.

F. Temperature variation procedures

To demonstrate general ideas about Ising coupling constant variation, we collected data at discrete temperatures and employed an experimental protocol to attenuate the effects of dynamic arrest. Equilibrium behavior was only truly achievable in lower temperature regimes.

At low temperatures, the dynamics were fast, and the samples rapidly equilibrated. Therefore, before every temperature change, we opted to allow the sample to equilibrate at the lowest temperature (in the antiferromagnetic phase). Thereafter, we ramped the sample temperature rapidly to a higher value, and we collected sample images following the realization of the higher temperature for ~12 min. After completion of the high-temperature video, we rapidly lowered the sample back to the lowest temperature and allowed the sample to equilibrate before initiating the next temperature jump.

A typical temperature cycle example follows below. We first chose a sample with particular H/D and L/D. We then cooled it to 21 °C and acquired video microscopy data. Next, the temperature was rapidly increased to a higher temperature (e.g., 31 °C), and another video stream was collected after the sample reached steady-state at this temperature. Then, the sample was cooled back to 21 °C; data were collected; and after equilibration, the jump cycle was repeated for other target temperatures. Note that this procedure generated the most data at 21 °C. Target temperatures were acquired in the following order: 31, 29, 27, 25, 23, and again at 31 °C. Although imperfect, this approach enabled us to start all samples in approximately the same fluctuating AF phase. Of course, the approach to steady-state, especially for high temperature samples, which do not equilibrate, is influenced by the microstates the system passes through during this process.

The same temperature cycling was repeated for different H/D. In total, we explored six different temperatures (21, 23, 25, 27, 29, 31 °C) at three different H/D, taking a series of images/movies at 27.5 fps for 20 000 frames (~12 min).

G. Numerical calculations

Calculation of the Ising coupling constant, βJ, requires numerical integration of $\mathcal{Z}(\{+\})$, $\mathcal{Z}(\{-\})$, and $\mathcal{Z}$. To this end, we developed a custom Python code to calculate integrals in quasi-1D and quasi-2D. For the calculations, the Boltzmann weight utilizes the depletion potential (defined in the supplementary material, Sec. S1), which depends on surfactant volume fraction (ϕ_d), micelle rod-length (ℓ), and diameter (d). The integrals thus depend on geometric parameters H, L, and D and surfactant parameters ϕ_d, ℓ, and d. Details about the numerical integrations are supplied in the supplementary material, Sec. S3.

IV. RESULTS AND DISCUSSION

A. Samples with small thickness-to-diameter ratio: Experiment and model comparison

1. Static structural properties

We first examine the buckled colloidal system under conditions where we expect the free-volume modeling to be most accurate, i.e., experiments with the smallest H/D (Fig. 6). In the low-temperature range, the static structural properties of this sample exhibit many anticipated features, notably a change in the sign of the coupling coefficient. At higher temperatures, the large depletion attraction to the sample walls introduces significant dynamic arrest, and therefore, these samples cannot fully equilibrate. In this subsection, we present and discuss findings about the static structure. Later, we will discuss dynamics and the behaviors of colloidal systems with larger H/D, which can deviate more from the model assumption of a static in-plane lattice.

Experimental images (Fig. 6) qualitatively show the basic effect. The structures evolve from distributions of short stripes and zigzags to clusters of the same spin, i.e., as the temperature is increased. More quantitatively, in Ising systems, when the spins are very weakly interacting, we expect that $\langle N_s \rangle = 3$. However, when the coupling becomes strong, the "ideal" Ising system behaves differently for antiferromagnetic ($J < 0$) vs paramagnetic/ferromagnetic interactions ($J > 0$). Ideal frustrated antiferromagnetic systems on a fixed lattice (and even on lattices that can mechanically deform) will exhibit $2 \le \langle N_s \rangle \lesssim 3$. As the temperature approaches zero, a frustrated antiferromagnet without lattice distortion will have $\langle N_s \rangle$ close to 2; for lattices that can deform, well-known stripe and zigzag configurations arise and also give $\langle N_s \rangle$ close to 2.[1,67,68] On the other hand, with a positive coupling constant ($J > 0$), the spins prefer to align parallel. For the paramagnetic phase ($0 < \beta J < 0.275$), we expect $3 \lesssim \langle N_s \rangle \lesssim 5$, and for the ferromagnetic phase ($\beta J \ge 0.275$), we expect $\langle N_s \rangle \gtrsim 5$.[38,80] Note that the largest changes of $\langle N_s \rangle$ per unit change of βJ occur in the paramagnetic phase.

In Fig. 5(b), both experimental data and model predictions are plotted vs the strength of the depletion attraction (βU_{min}). The data (solid and open circles) represent experimental measurements of $\langle N_s \rangle$. The black solid circles are derived from experiments where the particles freely move between the up and down states and the samples equilibrate. The open circles, by contrast, are derived from experiments at higher temperatures where attractive forces between

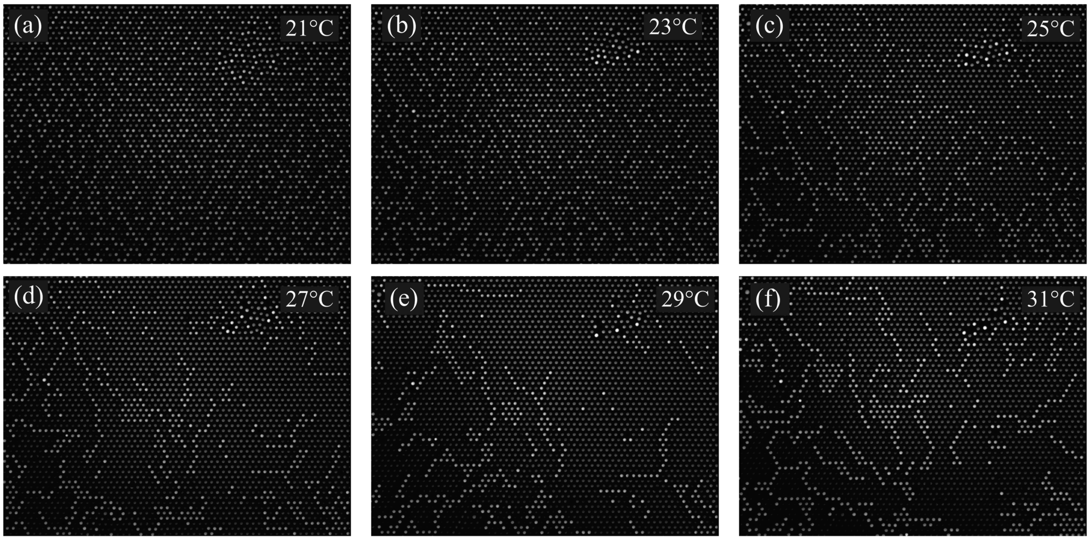

FIG. 6. Experimental images (contrast enhanced for visual clarity) of a buckled monolayer of colloidal spheres with temperature-dependent depletion interactions. The bright particles are buckled up with a spin assignment of $s_i = +1$, and the dark particles are buckled down with spin assignment $s_i = -1$. The data are from samples with confinement thickness, $H/D \sim 1.23$, at temperatures of (a) 21, (b) 23, (c) 25, (d) 27, (e) 29, and (f) 31 °C.

the particles and the walls are strong; in these cases, dynamic arrest hinders particle motion, and the samples do not equilibrate. On this plot, $\langle N_s \rangle$ is extracted from the experiment via particle tracking, and $U_{\min}$ is experimentally measured. Additionally, an expected βJ is extracted from Wannier's Ising model solution (right vertical axis) corresponding to $\langle N_s \rangle$ on the left vertical axis (Appendix D). The solid line is derived from our quasi-2D theoretical model, including wall interactions (see Sec. II A).

Figure 5(b) shows that at the lowest depletion attraction (lowest temperature), where $\beta U_{min} \approx -1.7$, the number of similar bonds $\langle N_s \rangle < 3$ and $\beta J < 0$. These samples are clearly in the antiferromagnetic phase. When the attraction is increased to $\beta U_{min} \approx -2.2$, then the number of similar bonds $\langle N_s \rangle \approx 3.2$ and $\beta J > 0$. These data demonstrate that the sample has evolved from the antiferromagnetic regime to the paramagnetic regime [Fig. 6(b)]. The experimental data thus show the Ising coupling constant transitions from negative to positive values, consistent with our theoretical model and exhibiting our primary expectation.

At higher attraction strengths where the depletion attraction becomes more dominant, $\beta U_{min} \approx -2.7$ to -4.3, $\langle N_s \rangle \approx 3.9$–$4.4$, and $\beta J \approx 0.19$–0.24. In this case, the system is approaching the paramagnetic–ferromagnetic crossover. Note, however, at 29 and 31 °C, the number of similar bonds stays nearly the same; this is because the large depletion attraction between the particles and walls induces dynamical arrest, preventing the sample from reaching equilibrium. Due to the dynamical arrest, the particles under these conditions do not flip enough to significantly rearrange. This effect prevents the observation of the P–F crossover. Model predictions deviate from experimental observations at high temperatures because arrested dynamics prevent equilibration.

The structural observations related to $\langle N_s \rangle$ provide experimental evidence for the crossover from one magnetic phase with $J < 0$ to another with $J > 0$. A second measurable morphological parameter worthy of quantitative exploration is the variance of $\langle N_s \rangle$, i.e., $\mathrm{var}(N_s) = \langle N_s^2 \rangle - \langle N_s \rangle^2$. The variance is plotted vs $\langle N_s \rangle$ in Fig. 7. In Fig. 7, the solid line shows the behavior predicted by the Ising model. The measured data for samples with all H/D are also shown. Here, we focus on the smallest H/D (blue triangles). At small and intermediate depletion attraction, its variance ranges from $\mathrm{var}(N_s) \approx 1.3$ to $\mathrm{var}(N_s) \approx 2.0$, following predictions of the Ising model in both the antiferromagnetic and paramagnetic regimes. At the higher temperatures, however, when the sample experiences dynamic arrest,

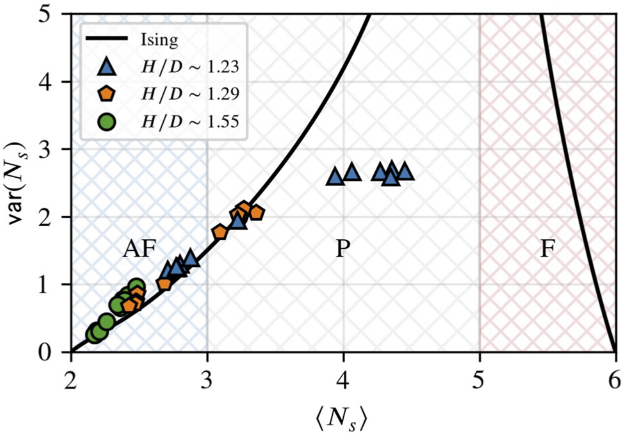

FIG. 7. Variance of the number of similar bonds $\mathrm{var}(N_s)$ vs the number of similar bonds $\langle N_s \rangle$. The solid line gives the predicted behavior based on the Ising model. Data for all samples are shown. The blue triangles, orange pentagons, and green circles show results for the samples with different H/D. AF, P, and F denote antiferromagnetic, paramagnetic, and ferromagnetic regimes.

$\mathrm{var}(N_s) \approx 2.7$; clearly, the samples in this higher temperature range have been quenched into local free energy minima with many particles remaining stuck at the walls. At these higher temperatures, we can visually confirm the paramagnetic phase ($J > 0$, below the P–F transition) from the presence of large clusters of particles with similar spin, but clearly, the high temperature samples are out-of-equilibrium and do not conform to expectations of the Ising model. Thus, the variance data for small H/D are largely consistent with our findings (and expectations) based on $\langle N_s \rangle$ alone.

2. Dynamics and structural arrest

We next examine the temporal dynamics of samples with $H/D = 1.23$. We focus on the simplest temporal fluctuations: single-particle spin-flip dynamics.

To quantitatively analyze spin-flip dynamics, we collect single-particle "spin" trajectories as a function of time. We determine $s_i(t)$ for each particle i in the video field-of-view. Using these trajectories, we compute the single-particle spin-flip temporal autocorrelation function,

$$C(t) = \frac{\langle s_i(t) s_i(0) \rangle - \langle s_i \rangle^2}{\langle s_i^2 \rangle - \langle s_i \rangle^2}. \tag{12}$$

Here, the angled brackets indicate averages over all particles. We fit the resultant curves to a stretched-exponential, $C(t) = \exp[-(t/\tau)^\gamma]$. From the fits, we extract a relaxation time, τ, and stretching factor, γ. The data and fitting results are shown in Fig. 8, and the corresponding best-fit parameters are tabulated in the supplementary material, Table S1. Stretched exponentials have $0 < \gamma < 1$ and can be indicative of heterogeneity amongst single-particle relaxation times.

When βU_{min} is comparatively small, $C(t)$ decays rapidly and is roughly exponential. In this regime, the relaxation time τ increases with depletion attraction strength (i.e., increasing temperature), and the temporal fluctuations are significant, enabling the system to reach equilibrium. At higher temperatures (starting for depletion attraction strength, $\beta U_{min} \approx -3.3$ at $T = 27\,^\circ\mathrm{C}$), the system becomes dynamically arrested. Dynamic arrest sets in when the system is deep in the paramagnetic regime, relatively close to the ferromagnetic phase.

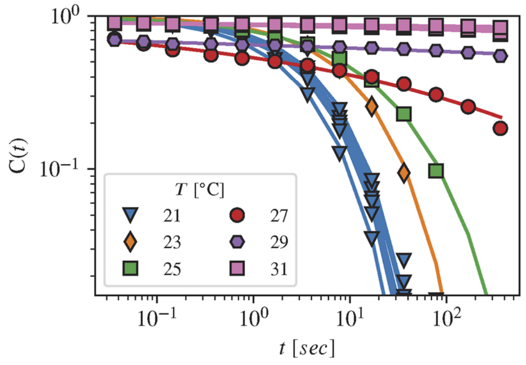

FIG. 8. Single-particle "spin" autocorrelation functions, $C(t)$ vs lag time t, along with stretched exponential best fits for $H/D = 1.23$. Note that a curve is obtained for each experiment; there are additional curves at 21 and 31 °C as a consequence of the repeated temperature jumps. Best fit parameters are tabulated in Table S1.

The attenuation of fluctuations at higher temperature is primarily due to the depletion attraction between the particles and the wall. This depletion attraction energy for particles near walls has been studied[73,77,81–84] and is expected to be approximately twice that of two colloidal particles in the bulk. The local energy barrier for wall escape (near both walls) becomes significant for $T > 27\,^\circ\mathrm{C}$, and the system is effectively quenched into a local minimum of the free energy landscape at some point during the sample processing (during the temperature jump). At the highest temperatures, the samples exhibit structures akin to frozen-in non-equilibrium paramagnetic phases. Dynamic arrest prevents transition to the ferromagnetic phase. Interestingly, wall interactions only slightly affect the equilibrium free energy (see dashed lines in Fig. 4), but they dramatically affect spin-flip rates. This phenomenology is consistent with the conclusions we arrived at from analysis of structural data. It provides an interesting physics contrast between the colloidal "magnetic" system and the atomic spin systems.

B. Samples with large wall separations

1. Static structural properties

In this final subsection, we summarize the behaviors of the colloidal systems with larger H/D ($H/D = 1.29$, 1.55). At larger H/D, the samples more readily accommodate lattice distortions, and therefore, their behavior will deviate from that of systems with a fixed in-plane lattice. As a result, we anticipate that the simple free-volume models will be *less realistic* for larger H/D, and the analogies to atomic Ising spin systems will be weaker. Nevertheless, these systems exhibit interesting similarities and differences compared to samples with $H/D = 1.23$ and the more idealized models. We first describe structural behavior.

For the system with $H/D = 1.29$, Figs. 9(a) and 9(b) provide images at different temperatures that qualitatively reveal the existence of a structural crossover where the coupling-constant changes sign. The images suggest evolution from the frustrated antiferromagnet to paramagnet. More quantitatively, for the lowest temperature (21 °C), $\beta U_{min} \approx -1.7$, $\langle N_s \rangle \approx 2.5$, and $\beta J \approx -0.29$. For the highest temperature (31 °C), $\langle N_s \rangle = 3.3$ at $\beta U_{min} \approx -4.3$, and $\beta J \approx 0.07$. The crossover from the negative to positive coupling constant occurs between 23 and 25 °C. This structural behavior is consistent with the theoretical expectation that the AF–P crossover transition will arise but will slightly shift (see Fig. 4) to occur at greater depletion attraction compared to samples with smaller H/D. When more free volume is accessible to the particles (with increasing H/D), the fraction of phase-space for which the depletion attraction is important is reduced, and the crossover shifts to require more depletion attraction.

The orange pentagons in Fig. 7 show the variance vs the number of similar bonds for $H/D = 1.29$. At low depletion attraction (21 °C) [Fig. 9(a)], $\langle N_s \rangle \approx 2.5$ and $\mathrm{var}(N_s) = 0.73$. This difference reflects a morphology of stripes and zig-zags that differs from that of samples with $H/D = 1.23$, which has shorter and more randomly oriented stripes. The observed small $\langle N_s \rangle$ and $\mathrm{var}(N_s)$ is consistent with the emergence of the zigzag-stripe ordered ground state that is expected to occur when lattice distortion can partially relieve

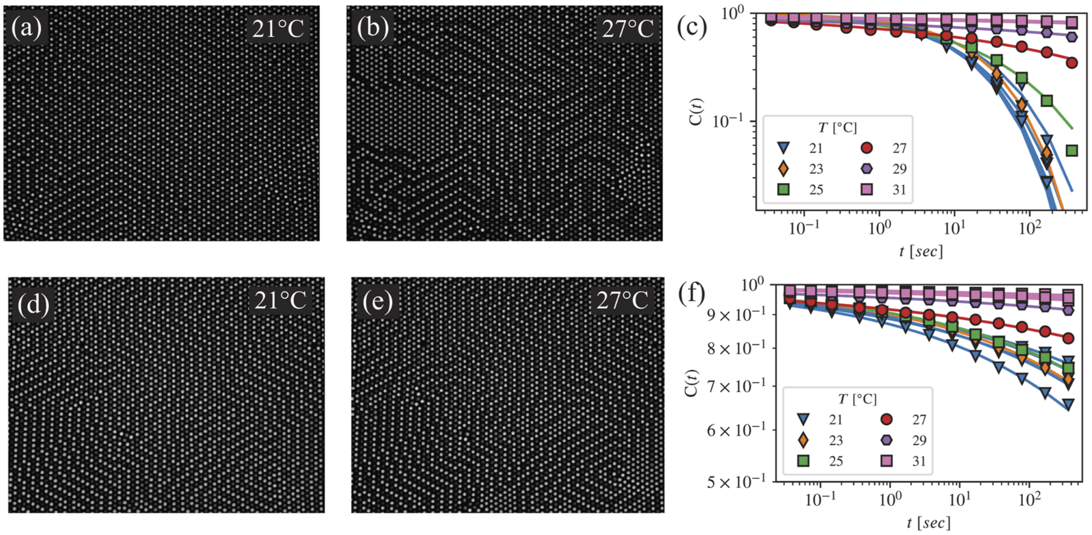

FIG. 9. Experimental images (contrast enhanced for visual clarity) of a buckled monolayer at wall-to-wall separation $H/D \sim 1.29$ [(a) and (b)] and $H/D \sim 1.55$ [(d) and (e)] at temperatures [(a) and (d)] 21 °C and [(b) and (e)] 27 °C. (c) and (f) Spin-flip autocorrelation functions for $H/D \approx 1.29$ and $H/D \approx 1.55$, respectively, with stretched exponential best-fits. Note that the vertical scales in (c) and (f) are *different*. Best fit parameters are tabulated in Table S1.

frustration.[88–90] The rest of the $\mathrm{var}(N_s)$ vs $\langle N_s\rangle$ data falls nicely on the predictions of the Ising model and exhibits the transition from a frustrated antiferromagnet to a paramagnet. At the highest temperature [Fig. 9(b)], the images show substantial clusters of buckled-up (or buckled-down) particles residing in the same plane, as might be expected in the paramagnetic phase, and traces of zigzag-stripe configurations perhaps where the lattice has distorted for some uncontrolled reason.

The system with $H/D = 1.55$ exhibits zigzag-stripe configurations exclusively [see Figs. 9(d) and 9(e)]. $\langle N_s\rangle < 3$ for all temperatures, and $\mathrm{var}(N_s) \approx 0.31 - 0.84$, is small for all temperatures (see green circles in Fig. 7). Superficially, the $\langle N_s\rangle$ and $\mathrm{var}(N_s)$ data fall roughly on the predicted Ising model curve, and the primary structural observations in the frustrated antiferromagnetic state are consistent with prior work.[1,67] However, in practice (see below), these samples experience dynamic arrest at all temperatures. More careful examination of Fig. 7 reveals significant fractional deviation from the Ising model predictions for relatively small $\langle N_s\rangle$ and $\mathrm{var}(N_s)$; the deviation is less obvious than the case of the smallest H/D sample in the paramagnetic regime perhaps because the fractional changes of $\langle N_s\rangle$ and $\mathrm{var}(N_s)$ per unit change of βJ are large in the paramagnetic regime.

2. Dynamic properties

Figure 9(c) shows spin-flip autocorrelation functions for $H/D = 1.29$ samples. These autocorrelation functions exhibit trends similar to those of the $H/D = 1.23$ sample. That is, we observe a low-temperature regime with roughly exponential dynamics that decay rapidly and thus allow the system to evolve to equilibrium states, but at higher temperatures, the samples exhibit dynamic arrest due to the depletion attraction of particles to the walls.

By contrast, the dynamics for the samples with $H/D = 1.55$ are very slow and non-exponential at all temperatures [see Fig. 9(f)]. This behavior is qualitatively different from the two systems with smaller H/D. The dynamics at low temperatures are slow because the system resides in the strongly frustrated antiferromagnet regime. The dynamics at the high temperatures are slow too, and like the samples with smaller H/D, this arrest effect is due to the strong depletion attraction of the particles to the walls. Thus, although the coupling constant varies with temperature, this system is quenched into deep minima of the frustrated antiferromagnet free energy landscape for all temperatures (but the dynamics are slow for different reasons at different temperatures). Again, the colloidal sample exhibits interesting differences with respect to traditional atomic magnetic systems.

V. CONCLUSIONS

In this contribution, we have shown how quasi-2D buckled colloidal monolayers on a triangular lattice can be induced to exhibit antiferromagnetic and para- and ferromagnetic behavior. A novel colloidal Ising system was created via the introduction of short-range, temperature-tunable entropic depletion attractions. Note that here we employed temperature-sensitive rod-like micelles as depletants, but, in principle, other depletants could work as well, e.g., microgel spheres whose size is temperature-dependent. We developed theoretical models with varying degrees of complexity that predict these effects, and we experimentally demonstrated the ideas using video microscopy. The structural experiments corroborated the central ideas. Additional dynamical measurements of sample spin-flip temporal autocorrelation functions showed that dynamic arrest is an intrinsic feature of the buckled colloid with depletion that arises when entropic attraction to the sample walls becomes important. The colloidal system thus offers interesting similarities and differences with respect to traditional atomic Ising systems and even to active matter systems[91,92] that are exciting to understand.

Another potentially interesting connection worth exploring concerns the similarities of the present system to glassy systems that exhibit the reentrant glass phenomenon,[17,18,25,26] e.g., which is also driven by increasingly strong depletion interactions.

In future experiments, it should be possible to ameliorate particle–wall attractions, which will facilitate cleaner studies of the nature of the crossover from one phase to another, as well as a better comparison of systems with rigid lattices vs deformable lattices. Moreover, it should be interesting to study "spin" structure and dynamics near defects, such as grain boundaries, and thereby examine the role of disorder in influencing relaxation, frustration, and phase behavior; potentially, it may even be possible to use optical traps to create systems that have some spin-glass character. Finally, deeper examination of system dynamics (beyond single-spin flipping) using analysis techniques developed for protein systems is under way and could prove interesting.

SUPPLEMENTARY MATERIAL

See the supplementary material for the analytical form of the pair potential (depletion potential), discussion of stuck particles, details of numerical calculations, and details of experimental measurements (i.e., βU_{min} measurement, L/D, H/D, and extracted fit parameters from spin-flip autocorrelation functions).

ACKNOWLEDGMENTS

We are happy to acknowledge many valuable discussions with Peter Collings, Yair Shokef, Piotr Habdas, Wei-Shao Wei, Alexis de la Cotte, Sophie Ettinger, Charlotte Slaughter, Winston Peloso, and Yihao Chen. We gratefully acknowledge the financial support from the U.S. National Science Foundation through Grant No. DMR2003659 (A.G.Y.) and the MRSEC under Grant No. DMR1720530, including its optical microscopy shared facility (A.G.Y.); the National Natural Science Foundation of China under Grant No. 1227041716 (X.M.); the National Key Research and Development Program of China under Grant No. 2022YFA1405002 (X.M.); the Stable Support Plan Program of Shenzhen Natural Science Fund under Grant No. 20220815094750002 (X.M.), and the Science and Engineering Research Board of Government of India under Grant No. SRG/2021/001077 (C.K.M.).

AUTHOR DECLARATIONS

Conflict of Interest

The authors have no conflicts to disclose.

Author Contributions

Analisa Hill: Conceptualization (lead); Data curation (lead); Formal analysis (lead); Investigation (lead); Methodology (lead); Software (lead); Validation (lead); Visualization (lead); Writing – original draft (lead); Writing – review & editing (lead). **Michio Tanaka**: Conceptualization (supporting); Formal analysis (supporting); Methodology (supporting); Software (supporting); Validation (lead); Visualization (supporting); Writing – review & editing (lead). **Kevin B. Aptowicz**: Conceptualization (supporting); Methodology (supporting); Visualization (supporting); Writing – review & editing (supporting). **Chandan K. Mishra**: Conceptualization (supporting); Methodology (supporting); Writing – review & editing (supporting). **Arjun G. Yodh**: Conceptualization (lead); Funding acquisition (lead); Methodology (lead); Project administration (lead); Resources (lead); Supervision (lead); Visualization (supporting); Writing – original draft (lead); Writing – review & editing (lead). **Xiaoguang Ma**: Conceptualization (lead); Methodology (lead); Project administration (equal); Supervision (supporting); Writing - review & editing (lead).

DATA AVAILABILITY

The data that support the findings of this study are available from the corresponding author upon reasonable request.

APPENDIX A: SPIN ASSIGNMENT

Bright and dark particles populate each image. Bright particles (near the top cover slip) are located in the microscope's focal plane, and the dark particles (near the bottom cover slip) are slightly out of focus. We determine the up–down assignments associated with the two "Ising" (buckled) states, $s_i \pm 1$, by creating a two-dimensional histogram of particle brightness (intensity), I, vs time. At each time, t, the ensemble of particle brightness' exhibits a bimodal distribution (see the supplementary material, Fig. S3). To assign a particle as "spin" up or down, a threshold brightness, $I_{\text{cut}}(t)$, is calculated using the two peaks in $I(t)$. In practice, we typically find that the two peaks are at the 25th and 75th percentiles of the $I(t)$ distribution; the up/down cut is set halfway between these two peaks. To check that our assignments are correct, we overlaid these assignments with experimental images and manually inspected them to confirm matching.

APPENDIX B: REALISTIC MODELS IN QUASI-2D: FORMULATION AND CALCULATIONS

In our more realistic calculation, the system free energy is computed from the product of the phase space of the central particle and that of its first nearest neighbors. This scheme requires averaging over all possible up/down configurations of the first and the second nearest neighbors of the central particle (see the supplementary material, Fig. S6). The second nearest neighbors must be included because the energy of a first nearest neighbor depends on the configuration of its own neighbors (which includes the central particle and some of the first and second nearest neighbors of the central particle). The realistic approach is briefly outlined below.

We first write the partition function for a single particle as a three-dimensional integral,

$$\mathcal{Z}(s_i;\mathcal{N}_i) = \int_{V(s_i,\mathcal{N}_i)} e^{-\beta U(\vec{r};\mathcal{N}_i)}\, d\vec{r}. \tag{B1}$$

Here, $\mathcal{N}_i$ represents the set of spins of the six nearest neighbors of particle i. $V(s_i,\mathcal{N}_i)$ is the volume of the cage made by the nearest neighbors of particle i; particle i is free to move in this cage but restricted to $z > H/2$ $(z \leq H/2)$ if $s_i = +1$ $(s_i = -1)$. $U(\vec{r}\mathcal{N}_i)$ is the potential felt by particle i at position $\vec{r}$ due to its six neighbors and the two walls (all of which, for our case, could be mediated via depletion interactions). To simplify the decoupling of this integral, we make the approximation that particle i's nearest neighbors remain exactly on their lattice positions at $z = H - D/2$ $(z = D/2)$ when their spins are $+1$ (-1).

We approximate the bulk partition function of N particles as a product over the partition function of each particle in the cage of its nearest neighbors,

$$\mathcal{Z}_{tot}(S) = \prod_{i}^{N} \mathcal{Z}(s_i; \mathcal{N}_i). \qquad \text{(B2)}$$

Here, S represents a specified set of all N spins spanning the system, and again, $\mathcal{N}_i$ is the set of six nearest neighbors of particle i.

The total free energy of the whole system is then

$$F(S) = -k_B T \log \mathcal{Z}_{tot}(S). \qquad \text{(B3)}$$

Our goal is to describe the system with an Ising model and to choose the optimal J such that the Ising energy term,

$$E(S; J) \equiv -J \sum_{\langle s_i s_j \rangle} s_i s_j, \qquad \text{(B4)}$$

provides a good approximation for $F(S)$ up to a constant independent of spin configuration. To accomplish this goal, we require that our Ising energy, with optimized J, should approximately capture the energy differences between any two global spin states (i.e., between "typical" global spin states) wherein only the central particle has flipped. We require

$$E(S_k^+; J) - E(S_k^-; J) \approx F(S_k^+) - F(S_k^-) \text{ for all } k. \qquad \text{(B5)}$$

Here, S_k^+ (S_k^-) denotes the global spin state wherein the central particle is up (down). The state of the remaining (neighboring) particles is indexed by k, which can take on one of 2^{N-1} possible configurations. Note that when Eq. (B5) is true, it follows that $F(S) \approx F(S; J) + \text{const}$ for all states S.

In writing single particle partition functions of the form in Eq. (B1), we have assumed that particles are free to move only within the cage of their *static* nearest neighbors whose z-positions are determined by their spins. Therefore, flipping the spin of the central particle affects only the partition function of the central particle and those of its six nearest neighbors. Furthermore, computation of the partition functions of the six nearest neighbors only requires knowledge of the spin state of the central particle and those of the 18 particles comprising the first and second nearest-neighbor rings.

Thus, to compute the free energy differences corresponding to a single spin flip, we need to only consider the combined 18 spins of the first and second nearest-neighbor rings. Accordingly, our state index k need to only index the state of these 18 particles and will take on one of 2^{18} possible configurations.

Our calculation task reduces to finding a value of J that best satisfies Eq. (B5) for all 2^{18} possible values of k. For each k, there is an optimal J_k, which we determine from

$$J_k = \frac{F(S_k^+) - F(S_k^-)}{\sum_{\langle ij \rangle} s_i s_j|_{S_k^+} - \sum_{\langle ij \rangle} s_i s_j|_{S_k^-}}. \qquad \text{(B6)}$$

As explained earlier, when the central particle flips, only the partition function of the central particle and those of its six nearest neighbors change. Accordingly, we can write $F(S_k^{\pm})$ in a form that involves a computable product of partition functions,

$$F(S_k^{\pm}) = -k_B T \log\left[\mathcal{Z}(\pm 1; \mathcal{N}) \prod_{i \in \mathcal{N}} \mathcal{Z}(s_i; \mathcal{N}_i)\right]. \qquad \text{(B7)}$$

Here, $\mathcal{N}$ represents the set of nearest neighbors of the central particle.

To compute the optimal J for the whole system, we average over all values of k (i.e., over all possible configurations of the 18 neighbors),

$$J = \frac{\sum_k J_k w_k}{\sum_k w_k}, \qquad \text{(B8)}$$

where

$$w_k \equiv \mathcal{Z}(S_k^+) + \mathcal{Z}(S_k^-) \qquad \text{(B9)}$$

is the Boltzmann weight for observing a particular configuration out to the second nearest neighbors; the weight accounts for cases where the center particle is up and down. This approach [Eq. (B8)] effectively incorporates the relative probability of observing each nearest-neighbor spin configuration.

Note that the above sums exclude k that correspond to spin states where three of the six central bonds are similar (i.e., frustrated for the antiferromagnet). For these nearest-neighbor configurations, there is no energy difference when the central particle flips, and the denominator of Eq. (B6) is zero. For examples of the above computations, see the supplementary material, Fig. S7.

APPENDIX C: PARAMAGNETIC TO FERROMAGNETIC TRANSITION

In Wannier's treatment of the triangular Ising antiferromagnet problem,[38] the Curie point, i.e., the transition between paramagnetic and ferromagnetic states, is given by setting μ, a convenience parameter defined by Wannier, equal to zero. μ is defined in Eq. (36) of Wannier's paper: $\mu = 1 - 2\tanh 2\beta J$. Solving for βJ, we get $\beta J = \frac{1}{2}\tanh^{-1}\frac{1}{2} \approx 0.275$. Thus, the value of βJ above which the system transitions to the ferromagnetic state is $\beta J \approx 0.275$. (Note that we have replaced Wannier's symbol L with βJ, and therefore, Wannier's definition of L is equivalent to our definition of βJ.)

APPENDIX D: RELATIONSHIP BETWEEN MEAN NUMBER OF SIMILAR BONDS ($\langle N_s \rangle$) AND WANNIER'S ENERGY EXPRESSION

Wannier derived an expression[80] for the total free energy of the system, U, normalized by $-\frac{2}{NJ}$ as a function of βJ: $f(\beta J) \equiv \frac{-2U}{NJ}$. Here, $U \equiv \frac{J}{2}\sum s_i s_j$ and i, j are neighboring spins that are summed over (note that Wannier's definition of J carries an extra factor of 2 compared to ours.) Additionally, $\sum s_i s_j = n_d - n_s$, where n_d (n_s) represents the total number of dissimilar (similar) bonds in the sample. Since every bond is either dissimilar or similar and since there are three bonds per N particles, $n_d = 3N - n_s$. (Note that the number of bonds *attached* to each particle is 6; however, in each unit cell, there is one particle and three bonds, so the number of bonds *per* particle is 3.) Thus, $\sum s_i s_j = 3N - 2n_s$, $U = \frac{J}{2}(3\ N - 2n_s)$, and $f(\beta J) = 2\frac{n_s}{N} - 3$. As defined in Sec. II B, $\langle N_s \rangle$ is the mean number of similar bonds attached to each particle, which has a maximum value of 6. Since $\langle N_s \rangle = 2n_s/N$, $\langle Ns \rangle$ can be related to Wannier's energy expression: $\langle Ns \rangle = f(\beta J) + 3$.

APPENDIX E: EXPERIMENTAL PHASE BEHAVIOR

With caveats about dynamic arrest, we attempted to combine all of the experimental data into a single plot (i.e., data from all H/D and temperatures). For this task, we started with the measured $\langle N_s \rangle$ for each H/D and temperature. For each measured $\langle N_s \rangle$, a one-to-one correspondence with βJ can be established using Wannier's theoretical calculation (see Appendix D). Note that by using $\langle N_s \rangle$ (rather than temperature) to characterize each experimental system, this data presentation is in some sense less sensitive to dynamic arrest; the arrested systems are effectively trapped at lower temperatures (with corresponding lower $\langle N_s \rangle$). The use of $\langle N_s \rangle$ thus approximately assigns an "equilibrium" state at a lower temperature to the sample.

Based on this approach, in the supplementary material, Fig. S5, we show a master plot of all samples (all possible H/D and temperatures). The master plot also contains Wannier's theory curve (Appendix D). With this plot, it is apparent that the experimental samples collectively span from the antiferromagnetic to paramagnetic regime (approaching the ferromagnetic regime). Thus, with caveats about the lack of equilibration due to dynamic arrest, this master plot further corroborates our central idea.

REFERENCES

[1] Y. Han, Y. Shokef, A. M. Alsayed, P. Yunker, T. C. Lubensky, and A. G. Yodh, "Geometric frustration in buckled colloidal monolayers," Nature **456**(7224), 898–903 (2008).

[2] B. Li, F. Wang, D. Zhou, Y. Peng, R. Ni, and Y. Han, "Modes of surface premelting in colloidal crystals composed of attractive particles," Nature **531**(7595), 485–488 (2016).

[3] Y. Han, N. Y. Ha, A. M. Alsayed, and A. G. Yodh, "Melting of two-dimensional tunable-diameter colloidal crystals," Phys. Rev. E **77**(4), 041406 (2008).

[4] A. E. Larsen and D. G. Grier, "Melting of metastable crystallites in charge-stabilized colloidal suspensions," Phys. Rev. Lett. **76**(20), 3862 (1996).

[5] A. M. Alsayed, M. F. Islam, J. Zhang, P. J. Collings, and A. G. Yodh, "Premelting at defects within bulk colloidal crystals," Science **309**(5738), 1207–1210 (2005).

[6] C. A. Murray and D. H. van Winkle, "Experimental observation of two-stage melting in a classical two-dimensional screened Coulomb system," Phys. Rev. Lett. **58**(12), 1200 (1987).

[7] C. A. Murray, W. O. Sprenger, and R. A. Wenk, "Comparison of melting in three and two dimensions: Microscopy of colloidal spheres," Phys. Rev. B **42**(1), 688 (1990).

[8] A. van Blaaderen, R. Ruel, and P. Wiltzius, "Template-directed colloidal crystallization," Nature **385**(6614), 321–324 (1997).

[9] J. J. Juárez, S. E. Feicht, and M. A. Bevan, "Electric field mediated assembly of three dimensional equilibrium colloidal crystals," Soft Matter **8**(1), 94–103 (2012).

[10] E. Kim, Y. Xia, and G. M. Whitesides, "Two-and three-dimensional crystallization of polymeric microspheres by micromolding in capillaries," Adv. Mater. **8**(3), 245–247 (1996).

[11] U. Gasser, E. R. Weeks, A. Schofield, P. N. Pusey, and D. A. Weitz, "Real-space imaging of nucleation and growth in colloidal crystallization," Science **292**(5515), 258–262 (2001).

[12] J. Taffs, S. R. Williams, H. Tanaka, and C. P. Royall, "Structure and kinetics in the freezing of nearly hard spheres," Soft Matter **9**(1), 297–305 (2013).

[13] J. L. Harland and W. van Megen, "Crystallization kinetics of suspensions of hard colloidal spheres," Phys. Rev. E **55**(3), 3054 (1997).

[14] P. Tan, N. Xu, and L. Xu, "Visualizing kinetic pathways of homogeneous nucleation in colloidal crystallization," Nat. Phys. **10**(1), 73–79 (2014).

[15] Y. Wang, Y. Wang, X. Zheng, É. Ducrot, J. S. Yodh, M. Weck, and D. J. Pine, "Crystallization of DNA-coated colloids," Nat. Commun. **6**(1), 7253 (2015).

[16] Y. Su, X. Ma, P.-Y. Lai, and P. Tong, "Colloidal diffusion over a quenched two-dimensional random potential," Soft Matter **13**(27), 4773–4785 (2017).

[17] C. K. Mishra, A. Rangarajan, and R. Ganapathy, "Two-step glass transition induced by attractive interactions in quasi-two-dimensional suspensions of ellipsoidal particles," Phys. Rev. Lett. **110**(18), 188301 (2013).

[18] T. Eckert and E. Bartsch, "Re-entrant glass transition in a colloid-polymer mixture with depletion attractions," Phys. Rev. Lett. **89**(12), 125701 (2002).

[19] E. D. Cubuk, R. J. S. Ivancic, S. S. Schoenholz, D. J. Strickland, A. Basu, Z. S. Davidson, J. Fontaine, J. L. Hor, Y.-R. Huang, Y. Jiang *et al.*, "Structure-property relationships from universal signatures of plasticity in disordered solids," Science **358**(6366), 1033–1037 (2017).

[20] D. Kaya, N. L. Green, C. E. Maloney, and M. F. Islam, "Normal modes and density of states of disordered colloidal solids," Science **329**(5992), 656–658 (2010).

[21] P. J. Yunker, K. Chen, M. D. Gratale, M. A. Lohr, T. Still, and A. G. Yodh, "Physics in ordered and disordered colloidal matter composed of poly(*n*-isopropylacrylamide) microgel particles," Rep. Prog. Phys. **77**(5), 056601 (2014).

[22] K. Chen, M. L. Manning, P. J. Yunker, W. G. Ellenbroek, Z. Zhang, A. J. Liu, and A. G. Yodh, "Measurement of correlations between low-frequency vibrational modes and particle rearrangements in quasi-two-dimensional colloidal glasses," Phys. Rev. Lett. **107**(10), 108301 (2011).

[23] X. Ma, Z. S. Davidson, T. Still, R. J. S. Ivancic, S. S. Schoenholz, A. J. Liu, and A. G. Yodh, "Heterogeneous activation, local structure, and softness in supercooled colloidal liquids," Phys. Rev. Lett. **122**(2), 028001 (2019).

[24] Z. Zhang, P. J. Yunker, P. Habdas, and A. G. Yodh, "Cooperative rearrangement regions and dynamical heterogeneities in colloidal glasses with attractive versus repulsive interactions," Phys. Rev. Lett. **107**(20), 208303 (2011).

[25] K. N. Pham, A. M. Puertas, J. Bergenholtz, S. U. Egelhaaf, A. Moussaïd, P. N. Pusey, A. B. Schofield, M. E. Cates, M. Fuchs, and W. C. K. Poon, "Multiple glassy states in a simple model system," Science **296**(5565), 104–106 (2002).

[26] X. Ma, C. K. Mishra, P. Habdas, and A. G. Yodh, "Structural and short-time vibrational properties of colloidal glasses and supercooled liquids in the vicinity of the re-entrant glass transition," J. Chem. Phys. **155**(7), 074902 (2021).

[27] M. D. Gratale, X. Ma, Z. S. Davidson, T. Still, P. Habdas, and A. G. Yodh, "Vibrational properties of quasi-two-dimensional colloidal glasses with varying interparticle attraction," Phys. Rev. E **94**(4), 042606 (2016).

[28] K. L. Galloway, X. Ma, N. C. Keim, D. J. Jerolmack, A. G. Yodh, and P. E. Arratia, "Scaling of relaxation and excess entropy in plastically deformed amorphous solids," Proc. Natl. Acad. Sci. U. S. A. **117**(22), 11887–11893 (2020).

[29] J. C. Crocker and D. G. Grier, "Methods of digital video microscopy for colloidal studies," J. Colloid Interface Sci. **179**(1), 298–310 (1996).

[30] P. Pieranski, L. Strzelecki, and B. Pansu, "Thin colloidal crystals," Phys. Rev. Lett. **50**(12), 900 (1983).

[31] M. Schmidt and H. Löwen, "Phase diagram of hard spheres confined between two parallel plates," Phys. Rev. E **55**(6), 7228 (1997).

[32] T. Chou and D. R. Nelson, "Buckling instabilities of a confined colloid crystal layer," Phys. Rev. E **48**(6), 4611 (1993).

[33] P. J. Yunker, M. Gratale, M. A. Lohr, T. Still, T. C. Lubensky, and A. G. Yodh, "Influence of particle shape on bending rigidity of colloidal monolayer membranes and particle deposition during droplet evaporation in confined geometries," Phys. Rev. Lett. **108**(22), 228303 (2012).

[34] S. Neser, C. Bechinger, P. Leiderer, and T. Palberg, "Finite-size effects on the closest packing of hard spheres," Phys. Rev. Lett. **79**(12), 2348 (1997).

[35] M. Schmidt and H. Löwen, "Freezing between two and three dimensions," Phys. Rev. Lett. **76**(24), 4552 (1996).

[36] A. Fortini and M. Dijkstra, "Phase behaviour of hard spheres confined between parallel hard plates: Manipulation of colloidal crystal structures by confinement," J. Phys.: Condens. Matter **18**(28), L371 (2006).
[37] H. Bock, K. E. Gubbins, and K. G. Ayappa, "Solid/solid phase transitions in confined thin films: A zero temperature approach," J. Chem. Phys. **122**(9), 094709 (2005).
[38] G. H. Wannier, "Antiferromagnetism. The triangular Ising net," Phys. Rev. **79**(2), 357 (1950).
[39] M. Mekata, "Antiferro-ferrimagnatic transition in triangular Ising lattice," J. Phys. Soc. Jpn. **42**(1), 76–82 (1977).
[40] M. Tsvetanova, K. Sotthewes, and H. J. W. Zandvliet, "Free energy of domain walls and order-disorder transition in a triangular lattice with anisotropic nearest-neighbor interactions," Phys. Rev. E **102**(3), 032138 (2020).
[41] J. Stephenson, "Ising-model spin correlations on the triangular lattice," J. Math. Phys. **5**(8), 1009–1024 (1964).
[42] W. Fang, A. Raeliarijaona, P.-H. Chang, A. A. Kovalev, and K. D. Belashchenko, "Spirals and skyrmions in antiferromagnetic triangular lattices," Phys. Rev. Mater. **5**(5), 054401 (2021).
[43] A. Libál, C. Reichhardt, and C. J. O. Reichhardt, "Realizing colloidal artificial ice on arrays of optical traps," Phys. Rev. Lett. **97**(22), 228302 (2006).
[44] P. Schiffer, A. P. Ramirez, D. A. Huse, and A. J. Valentino, "Investigation of the field induced antiferromagnetic phase transition in the frustrated magnet: Gadolinium gallium garnet," Phys. Rev. Lett. **73**(18), 2500 (1994).
[45] P. Schiffer, A. P. Ramirez, D. A. Huse, P. L. Gammel, U. Yaron, D. J. Bishop, and A. J. Valentino, "Frustration induced spin freezing in a site-ordered magnet: Gadolinium gallium garnet," Phys. Rev. Lett. **74**(12), 2379 (1995).
[46] M. J. P. Gingras, C. V. Stager, N. P. Raju, B. D. Gaulin, and J. E. Greedan, "Static critical behavior of the spin-freezing transition in the geometrically frustrated pyrochlore antiferromagnet $Y_2Mo_2O_7$," Phys. Rev. Lett. **78**(5), 947 (1997).
[47] J. S. Gardner, S. R. Dunsiger, B. D. Gaulin, M. J. P. Gingras, J. E. Greedan, R. F. Kiefl, M. D. Lumsden, W. A. MacFarlane, N. P. Raju, J. E. Sonier *et al.*, "Cooperative paramagnetism in the geometrically frustrated pyrochlore antiferromagnet $Tb_2Ti_2O_7$," Phys. Rev. Lett. **82**(5), 1012 (1999).
[48] Y. K. Tsui, C. A. Burns, J. Snyder, and P. Schiffer, "Magnetic field induced transitions from spin glass to liquid to long range order in a 3D geometrically frustrated magnet," Phys. Rev. Lett. **82**(17), 3532 (1999).
[49] O. A. Petrenko, C. Ritter, M. Yethiraj, and D. McK Paul, "Investigation of the low-temperature spin-liquid behavior of the frustrated magnet gadolinium gallium garnet," Phys. Rev. Lett. **80**(20), 4570 (1998).
[50] J. A. Hodges, P. Bonville, A. Forget, A. Yaouanc, P. Dalmas de Réotier, G. André, M. Rams, K. Królas, C. Ritter, P. C. M. Gubbens *et al.*, "First-order transition in the spin dynamics of geometrically frustrated $Yb_2Ti_2O_7$," Phys. Rev. Lett. **88**(7), 077204 (2002).
[51] R. Moessner and J. T. Chalker, "Properties of a classical spin liquid: The Heisenberg pyrochlore antiferromagnet," Phys. Rev. Lett. **80**(13), 2929 (1998).
[52] M. J. Harris, S. T. Bramwell, D. F. McMorrow, T. Zeiske, and K. W. Godfrey, "Geometrical frustration in the ferromagnetic pyrochlore $Ho_2Ti_2O_7$," Phys. Rev. Lett. **79**(13), 2554 (1997).
[53] S. T. Bramwell and M. J. P. Gingras, "Spin ice state in frustrated magnetic pyrochlore materials," Science **294**(5546), 1495–1501 (2001).
[54] R. F. Wang, C. Nisoli, R. S. Freitas, J. Li, W. McConville, B. J. Cooley, M. S. Lund, N. Samarth, C. Leighton, V. H. Crespi, and P. Schiffer, "Artificial 'spin ice'in a geometrically frustrated lattice of nanoscale ferromagnetic islands," Nature **439**(7074), 303–306 (2006).
[55] D. Zhou, F. Wang, B. Li, X. Lou, and Y. Han, "Glassy spin dynamics in geometrically frustrated buckled colloidal crystals," Phys. Rev. X **7**(2), 021030 (2017).
[56] K. Mitsumoto, C. Hotta, and H. Yoshino, "Spin-orbital glass transition in a model of a frustrated pyrochlore magnet without quenched disorder," Phys. Rev. Lett. **124**(8), 087201 (2020).
[57] K. Binder and A. P. Young, "Spin glasses: Experimental facts, theoretical concepts, and open questions," Rev. Mod. Phys. **58**(4), 801 (1986).
[58] R. P. Cowburn, "Probing antiferromagnetic coupling between nanomagnets," Phys. Rev. B **65**(9), 092409 (2002).
[59] Z. Ma, J. Wang, Z. Y. Dong, J. Zhang, S. Li, S. H. Zheng, Y. Yu, W. Wang, L. Che, K. Ran *et al.*, "Spin-glass ground state in a triangular-lattice compound $YbZnGaO_4$," Phys. Rev. Lett. **120**(8), 087201 (2018).
[60] S. H. Skjærvø, C. H. Marrows, R. L. Stamps, and L. J. Heyderman, "Advances in artificial spin ice," Nat. Rev. Phys. **2**(1), 13–28 (2020).
[61] I. Gilbert, C. Nisoli, and P. Schiffer, "Frustration by design," Phys. Today **69**(7), 54–59 (2016).
[62] A. Ortiz-Ambriz and P. Tierno, "Engineering of frustration in colloidal artificial ices realized on microfeatured grooved lattices," Nat. Commun. **7**(1), 10575 (2016).
[63] D. Y. Lee and P. Tierno, "Energetics and the ground state quest in an artificial triangular colloidal ice," Phys. Rev. Mater. **2**(11), 112601 (2018).
[64] B. Zhang, X. Chen, F. Deng, X. Lv, C. Zhang, B. Zheng, H. Wang, and J. Wang, "Spin direction tunable topological transition in two-dimensional frustrate antiferromagnetic triangular lattice T-FeO_2 monolayer," Appl. Phys. Lett. **121**(23), 232405 (2022).
[65] A. Ortiz-Ambriz, C. Nisoli, C. Reichhardt, C. J. O. Reichhardt, and P. Tierno, "Colloquium: Ice rule and emergent frustration in particle ice and beyond," Rev. Mod. Phys. **91**, 041003 (2019).
[66] K. Sotthewes and H. J. W. Zandvliet, "Universal behaviour of domain wall meandering," J. Phys.: Condens. Matter **25**(20), 205301 (2013).
[67] Y. Shokef and T. C. Lubensky, "Stripes, zigzags, and slow dynamics in buckled hard spheres," Phys. Rev. Lett. **102**(4), 048303 (2009).
[68] Y. Shokef, Y. Han, A. Souslov, A. G. Yodh, and T. C. Lubensky, "Buckled colloidal monolayers connect geometric frustration in soft and hard matter," Soft Matter **9**(29), 6565–6570 (2013).
[69] F. Leoni and Y. Shokef, "Attraction controls the entropy of fluctuations in isosceles triangular networks," Entropy **20**(2), 122 (2018).
[70] F. Leoni and Y. Shokef, "Attraction controls the inversion of order by disorder in buckled colloidal monolayers," Phys. Rev. Lett. **118**(21), 218002 (2017).
[71] D. Abutbul and D. Podolsky, "Topological order in an antiferromagnetic tetratic phase," Phys. Rev. Lett. **128**(25), 255501 (2022).
[72] Y. Shokef, A. Souslov, and T. C. Lubensky, "Order by disorder in the antiferromagnetic Ising model on an elastic triangular lattice," Proc. Natl. Acad. Sci. U. S. A. **108**(29), 11804–11809 (2011).
[73] A. D. Dinsmore, A. G. Yodh, and D. J. Pine, "Phase diagrams of nearly-hard-sphere binary colloids," Phys. Rev. E **52**(4), 4045 (1995).
[74] J. R. Savage, D. W. Blair, A. J. Levine, R. A. Guyer, and A. D. Dinsmore, "Imaging the sublimation dynamics of colloidal crystallites," Science **314**(5800), 795–798 (2006).
[75] J. R. Savage and A. D. Dinsmore, "Experimental evidence for two-step nucleation in colloidal crystallization," Phys. Rev. Lett. **102**(19), 198302 (2009).
[76] M. D. Gratale, T. Still, C. Matyas, Z. S. Davidson, S. Lobel, P. J. Collings, and A. G. Yodh, "Tunable depletion potentials driven by shape variation of surfactant micelles," Phys. Rev. E **93**(5), 050601 (2016).
[77] M. Piech and J. Y. Walz, "Depletion interactions produced by nonadsorbing charged and uncharged spheroids," J. Colloid Interface Sci. **232**(1), 86–101 (2000).
[78] S. Galam and P. V. Koseleff, "Solving the triangular Ising antiferromagnet by simple mean field," Eur. Phys. J. B **28**(2), 149–155 (2002).
[79] J. Adler, "Modern series analysis techniques and the relation to Monte-Carlo results on similar models," in *Computer Simulation Studies in Condensed-Matter Physics VIII* (Springer, 1995), pp. 5–17.
[80] G. H. Wannier, "Antiferromagnetism. The triangular Ising net," Phys. Rev. B **7**(11), 5017 (1973).
[81] A. D. Dinsmore, A. G. Yodh, and D. J. Pine, "Entropic control of particle motion using passive surface microstructures," Nature **383**(6597), 239–242 (1996).
[82] P. D. Kaplan, J. L. Rouke, A. G. Yodh, and D. J. Pine, "Entropically driven surface phase separation in binary colloidal mixtures," Phys. Rev. Lett. **72**(4), 582 (1994).
[83] M. Piech, P. Weronski, X. Wu, and J. Y. Walz, "Prediction and measurement of the interparticle depletion interaction next to a flat wall," J. Colloid Interface Sci. **247**(2), 327–341 (2002).

[84] H. N. W. Lekkerkerker and R. Tuinier, *Colloids and the Depletion Interaction* (Springer, 2011), Vol. 833.
[85] A. D. Dinsmore and A. G. Yodh, "Entropic confinement of colloidal spheres in corners on silicon substrates," Langmuir **15**(2), 314–316 (1999).
[86] Y. Mao, M. E. Cates, and H. N. W. Lekkerkerker, "Depletion stabilization by semidilute rods," Phys. Rev. Lett. **75**(24), 4548 (1995).
[87] J. Gapinski, J. Szymanski, A. Wilk, J. Kohlbrecher, P. Adam, and R. Hołyst, "Size and shape of micelles studied by means of SANS, PCS, and FCS," Langmuir **26**(12), 9304–9314 (2010).
[88] Z.-Y. Chen and M. Kardar, "Elastic antiferromagnets on a triangular lattice," J. Phys. C: Solid State Phys. **19**(34), 6825 (1986).
[89] L. Gu, B. Chakraborty, P. L. Garrido, M. Phani, and J. L. Lebowitz, "Monte Carlo study of a compressible Ising antiferromagnet on a triangular lattice," Phys. Rev. B **53**(18), 11985 (1996).
[90] S.-H. Lee, C. Broholm, T. H. Kim, W. Ratcliff, and S.-W. Cheong, "Local spin resonance and spin-peierls-like phase transition in a geometrically frustrated antiferromagnet," Phys. Rev. Lett. **84**(16), 3718 (2000).
[91] D. Nishiguchi, I. S. Aranson, A. Snezhko, and A. Sokolov, "Engineering bacterial vortex lattice via direct laser lithography," Nat. Commun. **9**(1), 4486 (2018).
[92] H. Wioland, F. G. Woodhouse, J. Dunkel, and R. E. Goldstein, "Ferromagnetic and antiferromagnetic order in bacterial vortex lattices," Nat. Phys. **12**(4), 341–345 (2016).